Check for updates

Atmospheric Science Letters

RMetS Royal Meteorological Society

RESEARCH ARTICLE OPEN ACCESS

Re-Intensification of Seafalling Tropical Cyclones

Enoch Yan Lok Tsui[1,2,3] | Ralf Toumi[1]

[1]Department of Physics, Imperial College London, London, UK | [2]Leverhulme Centre for Wildfires, Environment and Society, London, UK | [3]Atmosphere and Ocean Research Institute, The University of Tokyo, Chiba, Japan

Correspondence: Enoch Yan Lok Tsui (e.tsui20@imperial.ac.uk)

Received: 13 January 2025 | **Revised:** 24 July 2025 | **Accepted:** 8 September 2025

Funding: This work was supported by Leverhulme Centre for Wildfires, Environment and Society through the Leverhulme Trust (RC-2018-023), the Croucher Foundation, the Natural Environment Research Council (NE/W009587/1), and the Singapore Green Finance Centre.

Keywords: atmosphere–land interactions | atmospheric physics | geographic/climatic zone | numerical methods and NWP | ocean-atmosphere coupling | tools and methods | tropics | weather/climate extremes

ABSTRACT

The study of tropical cyclones re-entering the ocean or making 'seafall' has been limited. Here, idealised simulations are used to study the re-intensification of seafalling tropical cyclones. They follow a two-stage fast-slow process driven predominately by a change in surface friction initially and then by heating. The previous land decay causes seafalling tropical cyclones to be larger and intensify more slowly with milder inner-core contraction than in ocean-only cases. Nonetheless, they reach the same intensity but with almost twice the integrated kinetic energy, so that the second landfall made by seafalling tropical cyclones can cause more damage due to their larger footprint of destructive wind.

1 | Introduction

After making landfall, a tropical cyclone (TC) is cut off from the supply of heat and moisture from the ocean and experiences increased surface friction, generally leading to its weakening (Chen and Chavas 2020, 2021, 2023; Phillipson and Toumi 2021; Sparks and Toumi 2022a; Hlywiak and Nolan 2021; Takahashi and Nolan 2024; Takahashi et al. 2024). However, if such a perturbed system then re-enters the ocean (hereafter seafall), it can re-intensify. In fact, TCs in the western North Pacific and North Atlantic basins often pass over land and re-intensify over the ocean before making another landfall. For example, Typhoon Noru (2022) passed through Luzon Island before making landfall at Da Nang, Vietnam; Hurricane Ian (2022) passed through Cuba and then Florida before making its third and final landfall at Georgetown, South Carolina. They both re-intensified upon seafall (Wei et al. 2024; Heidarzadeh et al. 2023).

There are a handful of studies on the statistics of seafalling TCs in the western North Pacific. Brand and Blelloch (1973) and Brand and Blelloch (1974) are the first studies on seafalling TCs crossing the Philippines and Taiwan, respectively. They focused exclusively on the changes in TC characteristics such as intensity, size, translation speed, and track before and after passage over land. These statistics, while somewhat helpful for the operational forecaster, provide little insight regarding the physical processes driving the structural evolution and re-intensification of seafalling TCs.

The only mechanism proposed for the re-intensification of seafalling TCs is that of land-induced eyewall replacement as part of the following case studies by full simulation: Typhoon Zeb (1998) crossing the Philippines (Wu et al. 2009; Wu et al. 2003), Typhoon Megi (2010) crossing the Philippines (Wang and Wang 2014, 2021), Typhoon Fanapi (2010) crossing Taiwan (Yang et al. 2018), and Typhoon Mangkhut (2018) crossing the Philippines (Lau et al. 2024). However, only 57% of the TCs that cross the Philippines experience land-induced eyewall replacement, and the figure is even lower for TCs that cross Taiwan (Chou et al. 2011).

[Correction added on 16 October 2025, after first publication: The second affiliation has been corrected in this version due to a typographical error.]

This is an open access article under the terms of the Creative Commons Attribution License, which permits use, distribution and reproduction in any medium, provided the original work is properly cited.

© 2025 The Author(s). *Atmospheric Science Letters* published by John Wiley & Sons Ltd on behalf of Royal Meteorological Society.

It is therefore important to establish the general processes of TC seafall re-intensification. A clear understanding of the physics behind and the associated structural evolution of seafalling TCs is a first step to allow for better predictions of their behaviour leading up to the second landfall and could aid operational forecast and risk mitigation efforts.

2 | Methods

2.1 | Simulation Setup

The Weather Research and Forecasting (WRF) model version 4.4.1 (Skamarock et al. 2021) is used to run idealised simulations of TCs re-entering the ocean after spending time over land to study their seafall structural evolution. Two nested square domains with two-way interactions are used on an f-plane of fixed latitude. The inner domain with 802-by-802 grid cells and 3.999 km grid spacing (3207.198 km side length) is embedded in the outer domain with 600-by-600 grid cells and 11.997 km grid spacing (7198.2 km side length). The two domains are centre-aligned and both have 45 vertical levels, around 12 of which are below 2 km. The time steps of the inner and outer domains are 10 s and 30 s respectively.

An initial axisymmetric bogus vortex described by a near-surface tangential wind speed profile $V_0(r)$ detailed in Wang and Toumi (2019) is introduced into the model at the centre of the domains at the beginning. The initial bogus vortex is given a cyclonic sense of rotation and the wind speed tapers off linearly upwards from $V_0(r)$ near the surface to nil at an altitude of around 17 km. The initial environmental conditions and lateral boundary conditions throughout the simulation are given by the Jordan mean tropical sounding during hurricane seasons (Jordan 1958). No background wind is introduced into the model.

A full suite of physics parameterisations is used, including the WRF single-moment 6-class (WSM6) microphysics scheme (Hong and Lim 2006), the new Tiedtke cumulus scheme (Zhang and Wang 2017), the Rapid Radiative Transfer Model for general circulation models (RRTMG) scheme (Iacono et al. 2008) for both shortwave and longwave radiations, the Yonsei University (YSU) planetary boundary layer scheme (Hong et al. 2006), and the fifth-generation Pennsylvania State University-National Center for Atmospheric Research Mesoscale Model (MM5) similarity surface layer scheme (Grell et al. 1994; Fairall et al. 2003) with the four-layer unified Noah land surface model (Tewari et al. 2004). As the inner domain grid size of 3.999 km is fine enough to encapsulate most of the structure of the simulated TCs, the cumulus scheme is only applied to the outer domain. The chosen combination of physics parameterisations follows the National Center for Atmospheric Research Tropical Suite documented in the WRF User's Guide (Wang et al. 2022) to 'have been highly tested' and has been shown to capture well the structural details of TCs (e.g., Khaira and Astitha 2023).

2.2 | Experiment Design

The experiments begin with an 'ocean' run where the entire simulation domain is over an ocean surface with a fixed sea surface temperature (SST) of 29°C, the climatological SST around the Philippines (Magnaye et al. 2022) and Caribbean (Glenn et al. 2015) during TC season. An initial bogus vortex with $V_{0,\max} = 18\ \mathrm{m\,s^{-1}}$ and $R_{0,\max} = 100$ km is allowed to develop and mature over 12 days. The chosen $V_{0,\max}$ and $R_{0,\max}$ are commensurate with those of a weak and loose tropical storm to encourage the spontaneous development of a TC at the start of the simulation, providing TCs of varying initial states for landfall runs later. Then, a total of 5 landfall runs are initiated from the ocean run every 24 h beginning 4 days into the ocean run by switching the ocean surface in the entire domain into land making use of WRF's restart function. Such an algorithm has previously been successfully applied to study landfalling TCs with various numerical weather models including WRF (e.g., Sparks and Toumi 2022a; Li and Chakraborty 2021). Here, the land surface type of 'croplands' from the IGBP-modified MODIS 20-category land use categories is chosen in all landfall runs, each lasting 24 h. While no one single land use category dominates the Tropics, 'croplands' is commonly found in the Philippines and Caribbean (Friedl and Sulla-Menashe 2022; Sulla-Menashe et al. 2019) and its parameters are representative of the region. For example, the major land use categories there have roughness length and albedo of 0.05–0.5 m and 0.12–0.22, while those for 'croplands' are 0.15 m and 0.17. Finally, a total of 20 seafall runs, each lasting 72 h, are initiated 3, 9, 15 and 21 h into each landfall run by similarly switching the land in the entire domain back into ocean surface with a fixed SST of 29°C. Figure S1 details the surface history for each experiment. All simulations are performed at a latitude of 22.3° N.

To study the seafall re-intensification behaviour of the simulated TCs, the following properties of the TCs in both the ocean and seafall runs are determined hourly: the maximum near-surface wind speed ($V_{\max}$), the minimum surface pressure ($p_{\min}$), the radius of $V_{\max}$ ($R_{\max}$), the gradient wind speed at the point of $V_{\max}$ (V_{gwb}), the inflow angle at the point of $V_{\max}$ ($\alpha_{\max}$), the azimuthally averaged near-surface wind speed ($\widetilde{V}$), the radius of maximum $\widetilde{V}$ ($\widetilde{R}_{\max}$), the azimuthally averaged relative angular momentum per unit mass at $\widetilde{R}_{\max}$ with respect to the TC centre ($\widetilde{M}_{\max}$), the radius beyond $\widetilde{R}_{\max}$ at which $\widetilde{V}$ reaches gale force 34 kt (R_{34}), the integrated kinetic energy (IKE; Powell and Reinhold 2007) and the azimuthally averaged logarithmic reflectivity (Ladwig 2017) at an altitude of 5 km ($\widetilde{L}_Z^{5\mathrm{km}}$). The location of $p_{\min}$ is considered to be the TC centre; V_{gwb} is estimated by

$$V_{\mathrm{gwb}} = -\frac{fR_{\max}}{2} + \sqrt{\frac{f^2R_{\max}^2}{4} + \frac{R_{\max}\left|\nabla_{\mathrm{h}}p\right|}{\rho}}, \tag{1}$$

where f is the Coriolis parameter corresponding to the f-plane latitude of the simulation domain, $|\nabla_{\mathrm{h}}p|$ the magnitude of the horizontal gradient of pressure obtained using central difference and ρ the air density, both evaluated at the point of $V_{\max}$; $\alpha_{\max}$ (negative corresponding to inflow) is given by

$$\alpha_{\max} = \mathrm{atan2}\left(\vec{R}_{\max}\cdot\vec{V}_{\max}, \left|\vec{R}_{\max}\times\vec{V}_{\max}\right|\right), \tag{2}$$

where $\vec{R}_{\max}$ is the vector pointing from the TC centre to the point of $V_{\max}$ and $\vec{V}_{\max}$ the wind vector at the point of $V_{\max}$; and the IKE is integrated over the volume between 9.5 m and 10.5 m altitude

1530261x, 2025, 10, Downloaded from https://rmets.onlinelibrary.wiley.com/doi/10.1002/asl.1321 by Imperial College London, Wiley Online Library on [07/11/2025]. See the Terms and Conditions (https://onlinelibrary.wiley.com/terms-and-conditions) on Wiley Online Library for rules of use; OA articles are governed by the applicable Creative Commons License

with V above gale force. Furthermore, the rates of change of V_{max} ($\dot{V}_{max}$) and p_{min} ($\dot{p}_{min}$) over a specific time window are determined by linearly regressing the respective time series within that time window.

3 | Results

Figure 1 shows the time-evolution of V_{max}, p_{min} and R_{max} of the TC during the ocean, landfall and seafall runs in one experiment. Figure S2 shows the same for all runs. The initial intensification of the vortex in the ocean run lasts around 3 days as can be seen from both Figure 1a and Figure 1b. Meanwhile, its inner-core size as indicated by R_{max} first contracts from the initial assigned value of 100 km to around 20 km over the course of 3 days and then slowly expands to around 40 km over the following 9 days (Figures 1c and S2). The maximum V_{max} achieved under the environment of the experiment setup is around 120 kt, while the lowest p_{min} reached is around 925 hPa (Figure S1). Both landfall and seafall cause a two-stage evolution of V_{max}. After seafall, V_{max} first increases abruptly and then continues to intensify at a much more gradual rate. In contrast, the evolution of p_{min} after seafall is much smoother. While the intensity of the TCs in the seafall runs tends to relax to the value in the ocean run at the corresponding simulation time, the inner-core size tends to remain bigger.

The time-evolution of V_{max}, p_{min}, $\widetilde{R}_{max}$, V_{max}/V_{gwb}, α_{max}, R_{34} and $\widetilde{M}_{max}$ of the TC in the ocean run (5-h moving average) and the seafall runs (composite) are shown in Figure 2a–g. The average values of these variables between days 5 and 9 in the ocean run are also indicated as a reference, representative of the relaxation values in an ocean-only scenario. The seafall time series are shifted in the time domain so that the V_{max} 2 h after seafall matches the ocean run value. All variables except for p_{min} show an abrupt change within the first 2 h after seafall. It can be seen from Figure 2a that after the initial shock, seafalling TCs intensify at a reduced rate compared with the intensification in the ocean run from the same V_{max}. The seafalling TCs take around 30 h longer than in the ocean run to eventually settle at a similar V_{max}. Such reduced rate of intensification for seafalling TCs is also observed in terms of p_{min} (Figure 2b). After the initial shock, the $\widetilde{R}_{max}$, R_{34} and $\widetilde{M}_{max}$ of seafalling TCs are all higher than during the ocean run intensification by roughly 40 % (Figure 2c,f,g). Figure 2d shows that in the ocean run, V_{max} tends to settle at around $1.03V_{gwb}$ in the long run. By the time of seafall, V_{max} has dropped to around $0.82V_{gwb}$ (this adjustment is completed within 2 h of landfall (not shown)) but recovers to

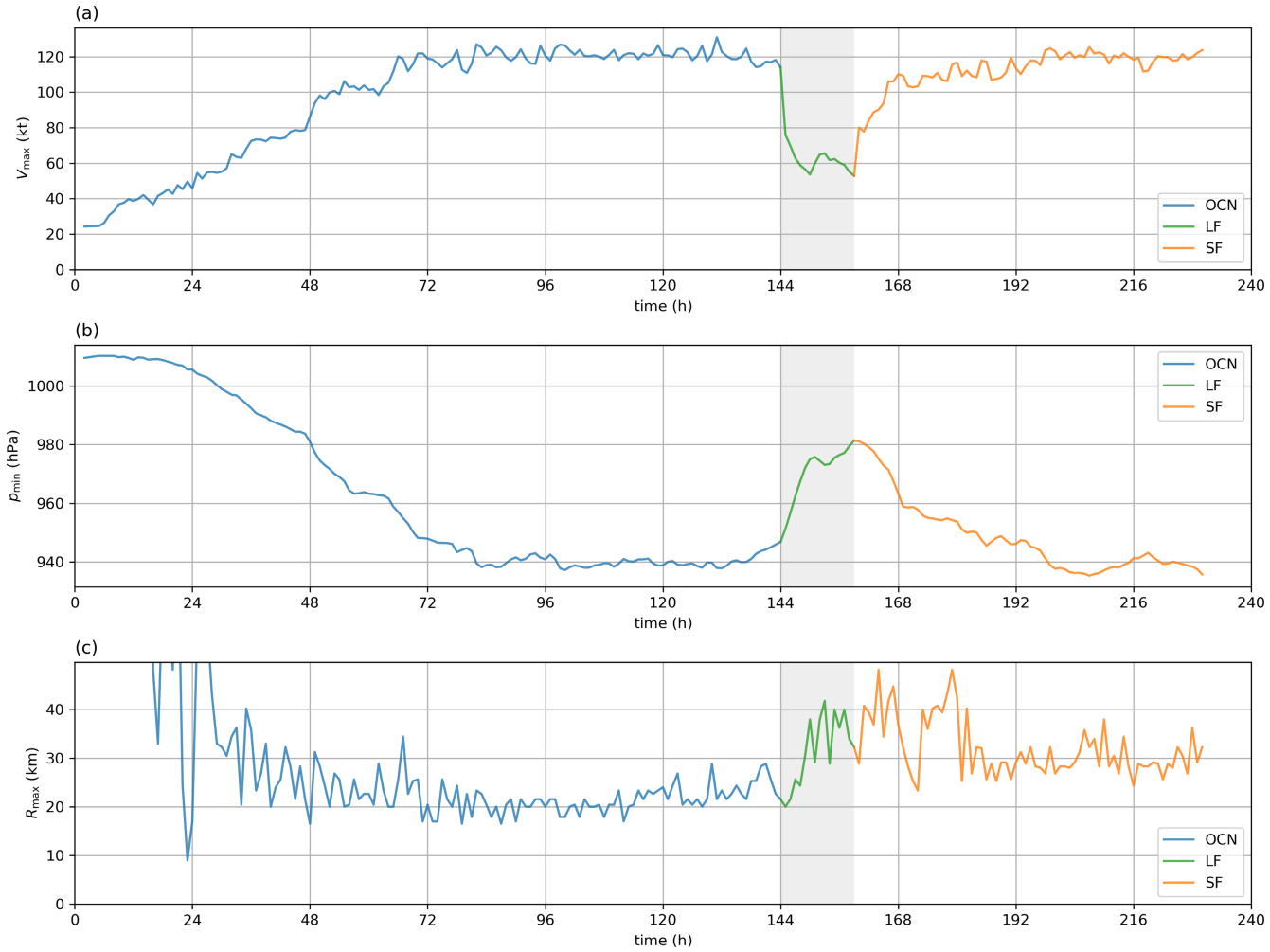


FIGURE 1 | Typical time-evolutions of (a) V_{max}, (b) p_{min} and (c) R_{max} during the ocean (OCN, blue), landfall (LF, green) and seafall (SF, orange) runs of the simulation. (a–c): Grey shading indicates the time during which the surface of the simulation domain is set to land.

1530261x, 2025, 10, Downloaded from https://rmets.onlinelibrary.wiley.com/doi/10.1002/asl.1321 by Imperial College London, Wiley Online Library on [07/11/2025]. See the Terms and Conditions (https://onlinelibrary.wiley.com/terms-and-conditions) on Wiley Online Library for rules of use; OA articles are governed by the applicable Creative Commons License

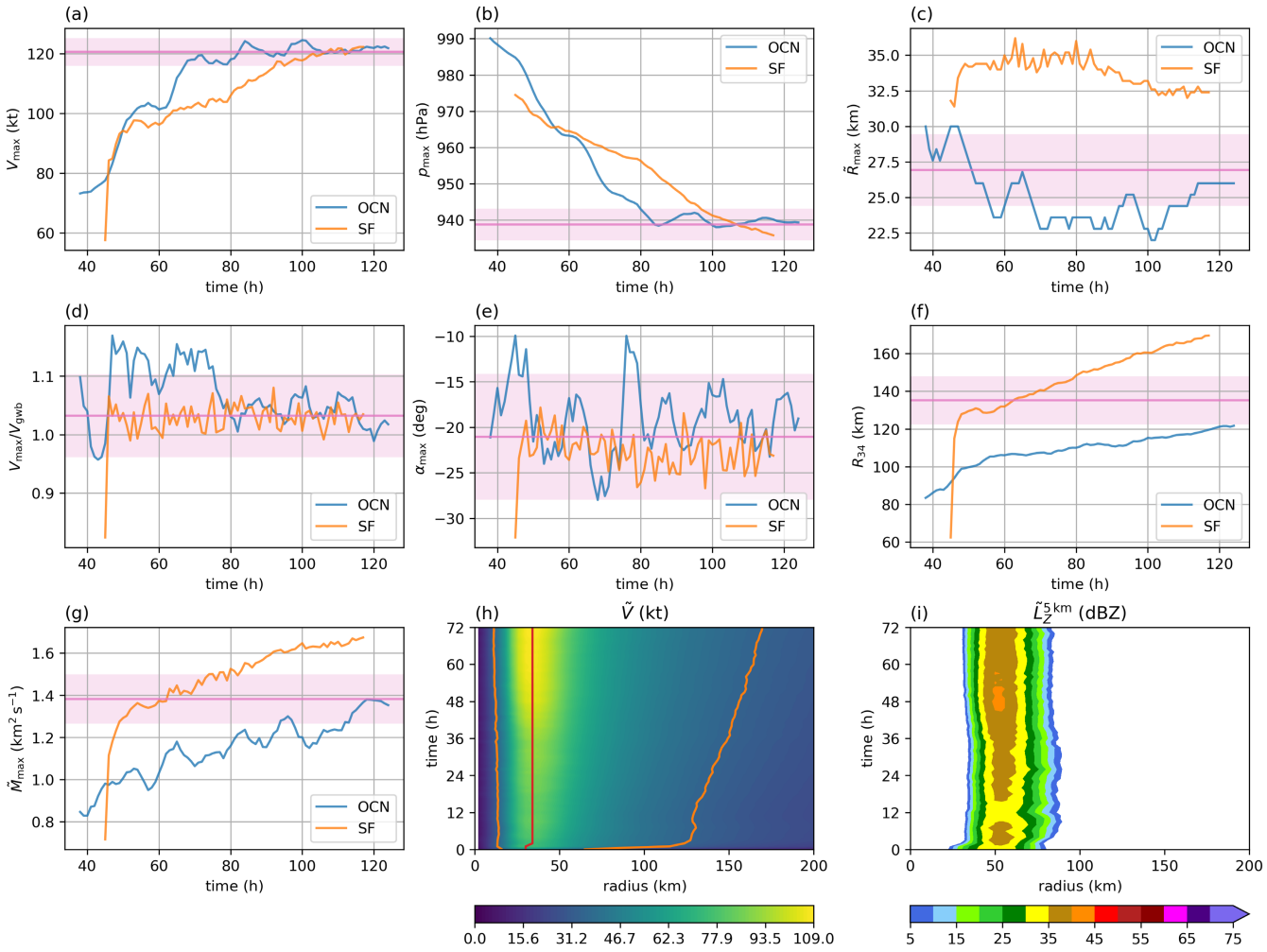


FIGURE 2 | Five-hour averaged ocean run (OCN) and composite seafall run (SF) time-evolution of (a) V_{max}, (b) p_{min}, (c) $\widetilde{R}_{max}$, (d) V_{max}/V_{gwb}, (e) α_{max}, (f) R_{34} and (g) $\widetilde{M}_{max}$. (a–g) Pink line indicates the corresponding value averaged between days 5 and 9 in the ocean run as a representative relaxation value developed purely over ocean, with shading covering one standard deviation on either side. (h) Hovmöller diagram of composite seafall $\widetilde{V}$. Orange line is the 34 kt contour; red line marks the maximum. (i) Same as (h) but for L_Z^{5km}.

around $1.03V_{gwb}$ within 2 h after seafall. Correspondingly, α_{max} at seafall is larger than in the ocean run but quickly settles around the ocean run value as shown in Figure 2e. Note that the quick recovery of V_{max}/V_{gwb} to its ocean run value within 2 h of seafall is due mainly to an abrupt leap of V_{max} as shown in Figure 2a while the change in p_{min} over this period is much more gradual as Figure 2b illustrates. The Hovmöller diagrams of composite seafall $\widetilde{V}$ and $\widetilde{L}_Z^{5km}$ are shown in Figure 2h,i. They suggest that land-induced eyewall replacement did not occur in the seafall runs of our experiment. This is confirmed with similar plots for individual seafall runs (not shown). Figure 2h,i are also consistent with Figure 2c,f that $\widetilde{R}_{max}$ is relatively stable but R_{34} keeps increasing for seafalling TCs after the initial shock.

To further study the differences in the intensification of seafalling and ocean-only TCs, the intensification rates, in terms of both V_{max} and p_{min}, in the seafall runs over the 24-h period starting 2 h after seafall, thereby avoiding the initial shock, are compared with the 24-h intensification rates in the ocean run starting from similar V_{max}. In Figure 3, the corresponding intensification rates are scattered against the initial V_{max} or p_{min}. The average $\widetilde{R}_{max}$, $\Delta\widetilde{R}_{max}$ and $\Delta\widetilde{M}_{max}$ over the 24-h period considered are also indicated. It is clear that TCs in the seafall runs have a lower intensification rate, both in terms of V_{max} and p_{min}, than in the ocean run for a similar intensity by around 0.7 kt h^{-1} or 0.6 hPa h^{-1}. It is further observed that the $\widetilde{R}_{max}$ (magnitude of $\Delta\widetilde{R}_{max}$) of TCs in the seafall runs are generally larger (smaller) than in the ocean run, with the difference increasing for stronger TCs. Meanwhile, the $\Delta\widetilde{M}_{max}$ of TCs of similar intensity in the seafall and ocean runs are somewhat similar, particularly for weaker TCs.

Figure 4a shows the time-evolution of the IKE of the TC in the ocean run (5-h moving average) and the seafall runs (composite), with the seafall time series shifted in the time domain so that the V_{max} 2 h after seafall matches the ocean run value. After the initial shock, the IKE of seafalling TCs is higher than during the ocean run intensification by roughly 50%, despite the lower intensification rate of seafalling TCs and hence their subsequently being weaker than in an ocean-only scenario (Figure 2a). By the time the seafalling TCs fully developed to the relaxation intensity in the ocean run, the IKE is almost double that in the ocean run. Figure 4b,c shows the scatter plots of IKE against V_{max} or p_{min} in the ocean and seafall runs, excluding the first 2 h after

1530261x, 2025, 10, Downloaded from https://rmets.onlinelibrary.wiley.com/doi/10.1002/asl.1321 by Imperial College London, Wiley Online Library on [07/11/2025]. See the Terms and Conditions (https://onlinelibrary.wiley.com/terms-and-conditions) on Wiley Online Library for rules of use; OA articles are governed by the applicable Creative Commons License

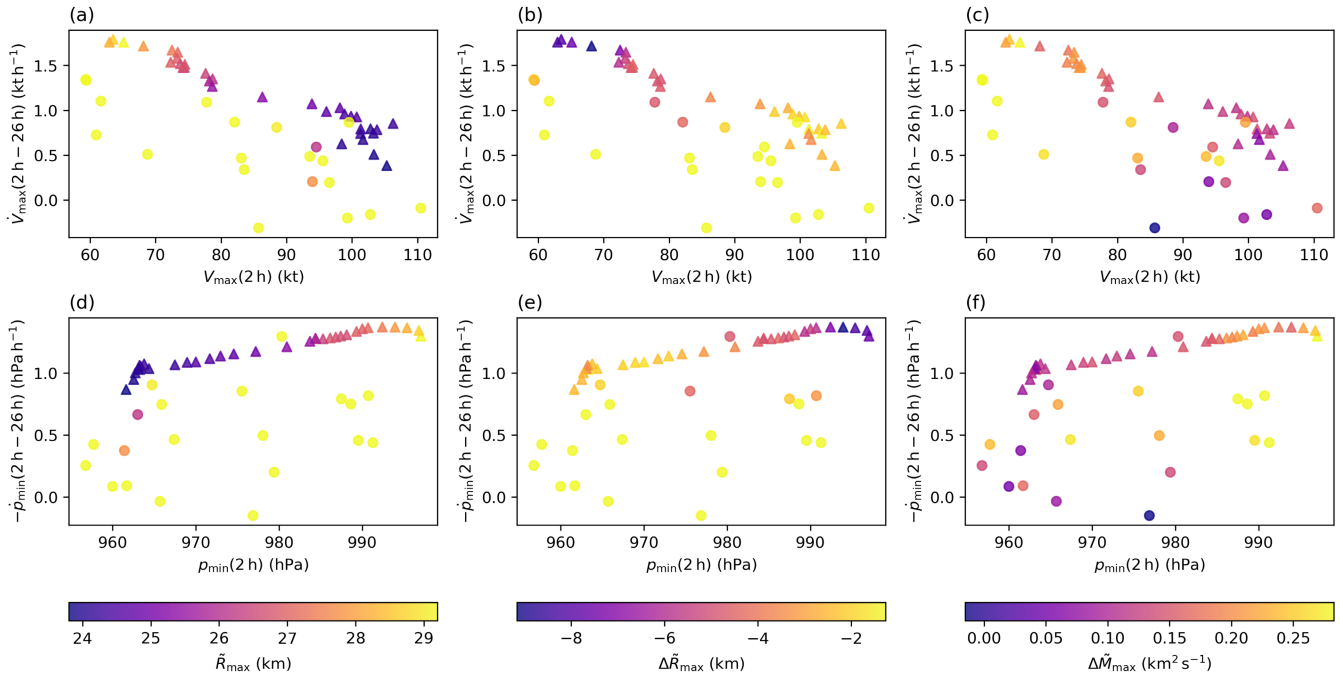


FIGURE 3 | (a) Scatter plot of 24-h rate of change of V_{max} against initial V_{max} 2 h post-seafall from each seafall run (circle) and corresponding rates for similar initial V_{max} from the ocean run (triangle). Marker colour shows the average $\widetilde{R}_{max}$ over the period. (d) Same as (a) but for the negative rate of change of p_{min} against initial p_{min}. (b, e) Same as (a, d) but with marker colour showing the change of $\widetilde{R}_{max}$ over the period. (c, f) Same as (a, d) but with maker colour showing the change of $\widetilde{M}_{max}$ over the period.

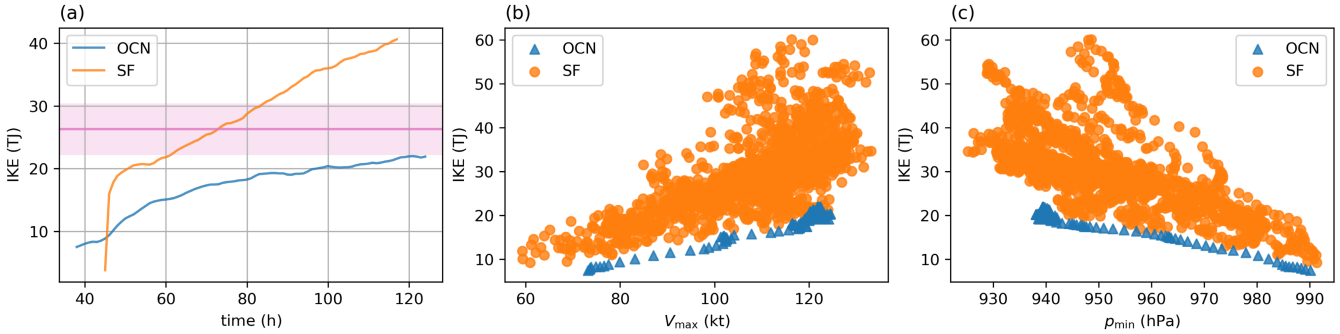


FIGURE 4 | (a) Same as Figure 2a but for IKE. (b) Scatter plot of IKE against V_{max} for the ocean (OCN, blue triangle) and seafall (SF, orange circle) runs. (c) Same as (b) but against p_{min}.

seafall. The IKE of TCs in the seafall runs is typically higher than in the ocean run by 80% for a similar intensity, both in terms of V_{max} and p_{min}.

4 | Discussion

Idealised numerical simulations produced by the WRF model are used to investigate the post-seafall behaviour of TCs, with a particular focus on their intensification. The experiment begins with an ocean run where a vortex is allowed to develop into a TC over an ocean surface with constant SST. The entire surface is then switched to land and then back to ocean at various times, producing landfall and seafall runs with TCs of varying initial states at seafall. In the ocean run, V_{max} fluctuates around 3% above V_{gwb} after the initial intensification (Figure 2d). This is indicative of near gradient wind balance and is consistent with the non-vanishing α_{max} (Figure 2e). By the time of seafall, V_{max} has decreased to around $0.82V_{gwb}$ accompanied by a bigger α_{max}, a clear indication that the near gradient wind balance is disrupted by the higher surface friction over land compared with ocean. Restoration of V_{max} back to the level of 3% above V_{gwb}, that is, the relaxation value in the ocean run, is achieved within 2 h of seafall (Figure 2d). This is accompanied by a decrease in α_{max} (Figure 2e) also to the relaxation value in the ocean run. Both suggest that gradient wind balance is restored to the level in an ocean-only scenario within 2 h of seafall. Land-induced eyewall replacement is absent in all of our seafall runs, unlike previous full simulation studies of real cases.

Seafalling TCs go through a two-stage structural evolution as they re-intensify. Immediately after seafall, V_{max} experiences an abrupt leap within 2 h (Figure 2a), aligning itself close to V_{gwb} (Figure 2d). Meanwhile, the change in p_{min} is much more gradual and lacks the abrupt leap akin to that experienced by V_{max}

1530261x, 2025, 10, Downloaded from https://rmets.onlinelibrary.wiley.com/doi/10.1002/asl.1321 by Imperial College London, Wiley Online Library on [07/11/2025]. See the Terms and Conditions (https://onlinelibrary.wiley.com/terms-and-conditions) on Wiley Online Library for rules of use; OA articles are governed by the applicable Creative Commons License

(Figure 2b). This suggests that the initial response to seafall from V_{max} is predominately due to a sharp decrease in surface friction. Afterwards, V_{max} continues to increase at a reduced rate compared with the initial intensification over ocean, and is accompanied by a gradual decrease in p_{min}. This subsequent, much more gradual, increase in V_{max} could then be understood as an intensification process driven thermodynamically as latent heat and moisture supply to the TC from a warm and moist ocean surface resumes.

Spending time over land causes TCs to not only weaken but also expand in both inner-core and outer sizes (Figure 2c,f). This is in agreement with Sparks and Toumi (2022a). Brand and Blelloch (1973) also observed eyewall expansion in TCs crossing the Philippines. Comparing TCs in our seafall runs with the ocean run at similar intensity, seafalling TCs have larger inner-core size and also intensify at a slower rate (Figure 3a,d). Emanuel (1989) and Sparks and Toumi (2022b) have both shown that larger TCs tend to intensify at a slower rate from a similar intensity. Emanuel (1989) argued, based on Emanuel and Rotunno (1989), that this behaviour in their simulations results from a greater proportion of the total energy being consumed to spin-up the larger anti-cyclone aloft a larger TC, leaving less energy to feed back to the surface fluxes. Sparks and Toumi (2022b) applied mass conservation and derived the dependence of the central pressure tendency of a TC on its inner-core size, central pressure and column inflow/outflow speed from their central pressure filling model considering only horizontal motion. They verified the resulting pressure–time relationship with observations. Consistent with these theories, seafalling TCs, with a larger inner-core, also have a slower intensification rate compared with the ocean run rate for a similar intensity (Figure 3a,d). Since angular momentum is the product of radius and tangential velocity, under similar change in $\widetilde{M}_{max}$ (Figure 3c,f), a more negative change in $\widetilde{R}_{max}$ (Figure 3b,e) implies a more positive change in $\widetilde{V}_{max}$. Indeed, the intensification of TCs is usually accompanied by a decrease in inner-core size (Shapiro and Willoughby 1982; Schubert and Hack 1983; Vigh and Schubert 2009). The larger inner-core and gentler contraction experienced by seafalling TCs hinder their intensification.

It is worth noting that seafalling TCs, despite their reduced rate of intensification, eventually reach the same intensity as in the ocean run but with a larger inner-core size and thus almost double the IKE (Figure 2a,c and Figure 4a). This higher IKE is caused by a larger footprint of destructive wind and is already apparent right after the initial shock following seafall when the seafalling and ocean-only TCs have the same intensity. This gap in IKE is sustained despite the ocean-only TC intensifying more quickly and widens as the intensity of the seafalling TCs eventually catches up. Wang and Toumi (2016) have shown a good relationship between US hurricane costs and IKE as well as other integrated metrics. This means that despite the initial maximum wind speed reduction due to the first landfall, seafalling TCs can have a greater economic impact at the second landfall even before they can then fully develop.

With the absence of land-induced eyewall replacement in our simulations, the results here can be directly applied to such seafalling TCs. These make up about half of the cases crossing the Philippines and Taiwan (Chou et al. 2011), while no similar statistics for the Atlantic basin is found in the literature. Notwithstanding, although eyewall replacement cycles encompass a weakening phase, the TC tends to eventually achieve the same or higher intensity with an expanded inner-core (Sitkowski et al. 2011), in line with the effects of land interactions on seafalling TCs observed here. Therefore, it is conceivable that our findings may also apply more broadly to seafalling TCs experiencing land-induced eyewall replacement. Lau et al. (2024) pointed out the important role played by complex topography in triggering the secondary eyewall formation in the seafalling Typhoon Mangkhut (2018). Wang et al. (2023) showed that a horizontal resolution of 2 km or finer is necessary to resolve secondary eyewall formation in idealised simulations. The lack of topography and choice of model resolution in our simulations could both have contributed to the absence of land-induced eyewall replacement here.

This study has demonstrated that previous interactions with land has a lasting impact on the structure of TCs even long after they have moved back over the ocean. In order for the unique behaviours of seafalling TCs, such as expanded inner-core and outer sizes and enhanced IKE, to be represented properly in operational forecasts, it is therefore important that forecast models are set up to allow for the transition between land and ocean to be captured accurately. Global models may struggle with their course resolution compared with regional models, in terms of both atmospheric gird size as well as land mass details, especially for cases with land-induced eyewall replacement.

5 | Conclusion

The re-intensification of seafalling TCs is investigated using idealised WRF simulations by switching the surface of the entire simulation domain from ocean to land and then back to ocean at various model times. Seafalling TCs undergo a two-stage fast-slow re-intensification process. Within 2 h of seafall, the restoration of gradient wind balance back to ocean-only level causes an abrupt jump of V_{max}. Subsequently, V_{max} continues to increase at a much slower rate, eventually reaching the value it would have in an ocean-only scenario but taking more time. Throughout the entire process, which lasts for around 2.5 days, p_{min} decreases smoothly without any abrupt leaps. The first stage is predominately a purely dynamical response of the seafalling TC to a sharp decrease in surface friction; while the second stage is a thermodynamically driven intensification process due to a resumption of latent heat and moisture supply from a warm and moist ocean surface. In the second stage, the intensification rate of the seafalling TC is always slower than in an ocean-only scenario for a similar intensity. This is likely a result of seafalling TCs having a larger inner-core size and being less capable of contracting owing to previous interactions with land. Finally, it is worth noting that seafalling TCs can represent a greater threat in the second landfall because of their larger footprint of destructive wind and higher IKE, even before being fully developed.

Author Contributions

Enoch Yan Lok Tsui: conceptualization, investigation, funding acquisition, writing – original draft, methodology, validation, visualization,

1530261x, 2025, 10, Downloaded from https://rmets.onlinelibrary.wiley.com/doi/10.1002/asl.1321 by Imperial College London, Wiley Online Library on [07/11/2025]. See the Terms and Conditions (https://onlinelibrary.wiley.com/terms-and-conditions) on Wiley Online Library for rules of use; OA articles are governed by the applicable Creative Commons License

writing – review and editing, software, formal analysis, data curation. **Ralf Toumi:** investigation, funding acquisition, methodology, validation, writing – review and editing, formal analysis, project administration, supervision, resources, conceptualization.

Acknowledgements

This study was supported by the Leverhulme Centre for Wildfires, Environment and Society through the Leverhulme Trust (RC-2018-023), the Croucher Foundation, the Natural Environment Research Council (NE/W009587/1) and the Singapore Green Finance Centre.

Conflicts of Interest

The authors declare no conflicts of interest.

Data Availability Statement

The data that support the findings of this study are available from the corresponding author upon reasonable request.

References

Brand, S., and J. W. Blelloch. 1973. "Changes in the Characteristics of Typhoons Crossing the Philippines." *Journal of Applied Meteorology* 12, no. 1: 104–109.

Brand, S., and J. W. Blelloch. 1974. "Changes in the Characteristics of Typhoons Crossing the Island of Taiwan." *Monthly Weather Review* 102, no. 10: 708–713.

Chen, J., and D. R. Chavas. 2020. "The Transient Responses of an Axisymmetric Tropical Cyclone to Instantaneous Surface Roughening and Drying." *Journal of the Atmospheric Sciences* 77, no. 8: 2807–2834.

Chen, J., and D. R. Chavas. 2021. "Can Existing Theory Predict the Response of Tropical Cyclone Intensity to Idealized Landfall?" *Journal of the Atmospheric Sciences* 78, no. 10: 3281–3296.

Chen, J., and D. R. Chavas. 2023. "A Model for the Tropical Cyclone Wind Field Response to Idealized Landfall." *Journal of the Atmospheric Sciences* 80, no. 4: 1163–1176.

Chou, K. H., C. C. Wu, and Y. Wang. 2011. "Eyewall Evolution of Typhoons Crossing the Philippines and Taiwan: An Observational Study." *Terrestrial, Atmospheric and Oceanic Sciences* 22, no. 6: 535.

Emanuel, K. A. 1989. "The Finite-Amplitude Nature of Tropical Cyclogenesis." *Journal of the Atmospheric Sciences* 46, no. 22: 3431–3456.

Emanuel, K. A., and R. Rotunno. 1989. "Polar Lows as Arctic Hurricanes." *Tellus A* 41A, no. 1: 1.

Fairall, C. W., E. F. Bradley, J. E. Hare, A. A. Grachev, and J. B. Edson. 2003. "Bulk Parameterization of Air-Sea Fluxes: Updates and Verification for the COARE Algorithm." *Journal of Climate* 16, no. 4: 571–591.

Friedl, M., and D. Sulla-Menashe. 2022. *Modis/Terra+Aqua Land Cover Type Yearly l3 Global 500 m Sin Grid v061*. NASA Land Processes Distributed Active Archive Center. https://doi.org/10.5067/MODIS/MCD12Q1.061.

Glenn, E., D. Comarazamy, J. E. González, and T. Smith. 2015. "Detection of Recent Regional Sea Surface Temperature Warming in the Caribbean and Surrounding Region." *Geophysical Research Letters* 42, no. 16: 6785–6792.

Grell, G. A., J. Dudhia, and D. R. Stauffer. 1994. "A Description of the Fifth-Generation Penn State/NCAR Mesoscale Model (MM5) (No. NCAR/TN-398+STR)." https://doi.org/10.5065/D60Z716B.

Heidarzadeh, M., T. Iwamoto, J. Šepić, and I. E. Mulia. 2023. "Normal and Reverse Storm Surges Along the Coast of Florida During the September 2022 Hurricane Ian: Observations, Analysis, and Modelling." *Ocean Modelling* 185: 102250.

Hlywiak, J., and D. S. Nolan. 2021. "The Response of the Near-Surface Tropical Cyclone Wind Field to Inland Surface Roughness Length and Soil Moisture Content During and After Landfall." *Journal of the Atmospheric Sciences* 78, no. 3: 983–1000.

Hong, S. Y., and J.-O. J. Lim. 2006. "The WRF Single-Moment 6-Class Microphysics Scheme (WSM6)." *Journal of the Korean Meteorological Society* 42, no. 2: 129–151.

Hong, S. Y., Y. Noh, and J. Dudhia. 2006. "A New Vertical Diffusion Package With an Explicit Treatment of Entrainment Processes." *Monthly Weather Review* 134, no. 9: 2318–2341.

Iacono, M. J., J. S. Delamere, E. J. Mlawer, M. W. Shephard, S. A. Clough, and W. D. Collins. 2008. "Radiative Forcing by Long-Lived Greenhouse Gases: Calculations With the AER Radiative Transfer Models." *Journal of Geophysical Research-Atmospheres* 113, no. 13: 2008JD009944.

Jordan, C. L. 1958. "Mean Soundings for the West Indies Area." *Journal of Meteorology* 15, no. 1: 91–97.

Khaira, U., and M. Astitha. 2023. "Exploring the Real-Time WRF Forecast Skill for Four Tropical Storms, Isaias, Henri, Elsa and Irene, as They Impacted the Northeast United States." *Remote Sensing* 15, no. 13: 3219.

Ladwig, W. 2017. *wrf-python (Version 1.2.0)*. UCAR/NCAR. https://doi.org/10.5065/D6W094P1.

Lau, K. H., C. Y. Tam, and C. C. Wu. 2024. "Island-Induced Eyewall Replacement in a Land-Falling Tropical Cyclone: A Model Study of Super Typhoon Mangkhut (2018)." *Journal of Geophysical Research: Atmospheres* 129, no. 4: e2023JD039541.

Li, L., and P. Chakraborty. 2021. "Birth of a Cold Core in Tropical Cyclones Past Landfall." *Physical Review Fluids* 6, no. 5: L051801.

Magnaye, A. M. T., G. T. Narisma, F. T. Cruz, et al. 2022. "Potential Influence of Sea Surface Temperature Representation in Climate Model Simulations Over CORDEX-SEA Domain." *International Journal of Climatology* 42, no. 7: 3702–3725.

Phillipson, L. M., and R. Toumi. 2021. "A Physical Interpretation of Recent Tropical Cyclone Post-Landfall Decay." *Geophysical Research Letters* 48, no. 18: e2021GL094105.

Powell, M. D., and T. A. Reinhold. 2007. "Tropical Cyclone Destructive Potential by Integrated Kinetic Energy." *Bulletin of the American Meteorological Society* 88, no. 4: 513–526.

Schubert, W. H., and J. J. Hack. 1983. "Transformed Eliassen Balanced Vortex Model." *Journal of the Atmospheric Sciences* 40, no. 6: 1571–1583.

Shapiro, L. J., and H. E. Willoughby. 1982. "The Response of Balanced Hurricanes to Local Sources of Heat and Momentum." *Journal of the Atmospheric Sciences* 39, no. 2: 378–394.

Sitkowski, M., J. P. Kossin, and C. M. Rozoff. 2011. "Intensity and Structure Changes During Hurricane Eyewall Replacement Cycles." *Monthly Weather Review* 139, no. 12: 3829–3847.

Skamarock, W. C., J. B. Klemp, J. Dudhia, et al. 2021. "A Description of the Advanced Research WRF Model Version 4.3 (No. NCAR/TN-556+STR)." https://doi.org/10.5065/1dfh-6p97.

Sparks, N., and R. Toumi. 2022a. "A Physical Model of Tropical Cyclone Central Pressure Filling at Landfall." *Journal of the Atmospheric Sciences* 79, no. 10: 2585–2599.

Sparks, N., and R. Toumi. 2022b. "The Dependence of Tropical Cyclone Pressure Tendency on Size." *Geophysical Research Letters* 49, no. 19: e2022GL098926.

Sulla-Menashe, D., J. M. Gray, S. P. Abercrombie, and M. A. Friedl. 2019. "Hierarchical Mapping of Annual Global Land Cover 2001 to

1530261x, 2025, 10, Downloaded from https://rmets.onlinelibrary.wiley.com/doi/10.1002/asl.1321 by Imperial College London, Wiley Online Library on [07/11/2025]. See the Terms and Conditions (https://onlinelibrary.wiley.com/terms-and-conditions) on Wiley Online Library for rules of use; OA articles are governed by the applicable Creative Commons License

Present: The MODIS Collection 6 Land Cover Product." *Remote Sensing of Environment* 222: 183–194.

Takahashi, T., and D. S. Nolan. 2024. "The Vortex Structure and Near-Surface Winds of Typhoon Faxai (2019) During Landfall. Part I: Observational Analysis." *Quarterly Journal of the Royal Meteorological Society* 150, no. 759: 1172–1193.

Takahashi, T., D. S. Nolan, and B. D. McNoldy. 2024. "The Vortex Structure and Near-Surface Winds of Typhoon Faxai (2019) During Landfall. Part II: Evaluation of WRF Simulations." *Quarterly Journal of the Royal Meteorological Society* 150, no. 760: 1643–1667.

Tewari, M., F. Chen, W. Wang, et al. 2004. "Implementation and Verification of the Unified Noah Land Surface Model in the WRF Model." http://ams.confex.com/ams/84Annual/techprogram/paper_69061.htm.

Vigh, J. L., and W. H. Schubert. 2009. "Rapid Development of the Tropical Cyclone Warm Core." *Journal of the Atmospheric Sciences* 66, no. 11: 3335–3350.

Wang, H., and Y. Wang. 2014. "A Numerical Study of Typhoon Megi (2010). Part I: Rapid Intensification." *Monthly Weather Review* 142, no. 1: 29–48.

Wang, H., and Y. Wang. 2021. "A Numerical Study of Typhoon Megi (2010). Part II: Eyewall Evolution Crossing the Luzon Island." *Monthly Weather Review* 149, no. 2: 375–394.

Wang, S., and R. Toumi. 2016. "On the Relationship Between Hurricane Cost and the Integrated Wind Profile." *Environmental Research Letters* 11, no. 11: 114005.

Wang, S., and R. Toumi. 2019. "Impact of Dry Midlevel Air on the Tropical Cyclone Outer Circulation." *Journal of the Atmospheric Sciences* 76, no. 6: 1809–1826.

Wang, W., C. Bruyère, M. Duda, et al. 2022. "User's Guide for the Advanced Research WRF (ARW) Modeling System, Version 4." https://www2.mmm.ucar.edu/wrf/users/docs/user_guide_v4/contents.html.

Wang, X., F. Weng, W. Peng, H. Zhang, and Q. Li. 2023. "Impact of Model Resolution on Secondary Eyewall Formation and Eyewall Replacement Cycle." *Journal of Advances in Modeling Earth Systems* 15, no. 2: e2022MS003175.

Wei, Y., Y. Chen, B. Zhao, et al. 2024. "Assimilation of New Rocket Dropsonde Data Using WRFDA and Its Impact on Numerical Simulations of Typhoon NORU." *Ocean Modelling* 189: 102343.

Wu, C. C., H. J. Cheng, Y. Wang, and K. H. Chou. 2009. "A Numerical Investigation of the Eyewall Evolution in a Landfalling Typhoon." *Monthly Weather Review* 137, no. 1: 21–40.

Wu, C. C., K. H. Chou, H. J. Cheng, and Y. Wang. 2003. "Eyewall Contraction, Breakdown and Reformation in a Landfalling Typhoon." *Geophysical Research Letters* 30, no. 17: 1887.

Yang, M. J., Y. C. Wu, and Y. C. Liou. 2018. "The Study of Inland Eyewall Reformation of Typhoon Fanapi (2010) Using Numerical Experiments and Vorticity Budget Analysis." *Journal of Geophysical Research: Atmospheres* 123, no. 17: 9604–9623.

Zhang, C., and Y. Wang. 2017. "Projected Future Changes of Tropical Cyclone Activity Over the Western North and South Pacific in a 20-km-Mesh Regional Climate Model." *Journal of Climate* 30, no. 15: 5923–5941.

Supporting Information

Additional supporting information can be found online in the Supporting Information section. **Figure S1:** Simulation domain surface history for all 20 experiments. **Figure S2:** Overview of the ocean, landfall and seafall runs for all 20 experiments, showing the time-evolutions of V_{max}, p_{min} and R_{max}.

1530261x, 2025, 10, Downloaded from https://rmets.onlinelibrary.wiley.com/doi/10.1002/asl.1321 by Imperial College London, Wiley Online Library on [07/11/2025]. See the Terms and Conditions (https://onlinelibrary.wiley.com/terms-and-conditions) on Wiley Online Library for rules of use; OA articles are governed by the applicable Creative Commons License